

pubs.acs.org/biochemistry Article

Kinetic and Structural Characterization of a Flavin-Dependent Putrescine N-Hydroxylase from Acinetobacter baumannii

Noah S. Lyons, Alexandra N. Bogner, John J. Tanner,* and Pablo Sobrado*



Cite This: Biochemistry 2022, 61, 2607-2620



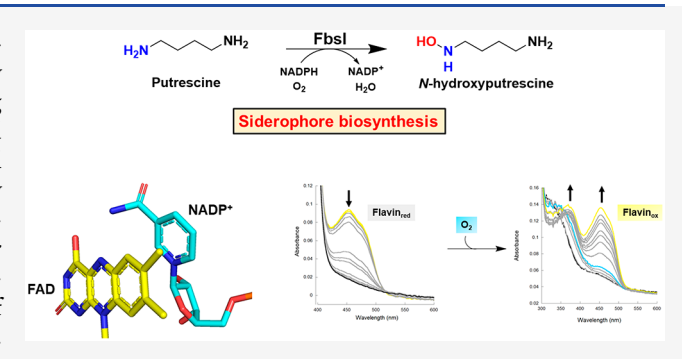
ACCESS

III Metrics & More

Article Recommendations

s Supporting Information

ABSTRACT: Acinetobacter baumannii is a Gram-negative opportunistic pathogen that causes nosocomial infections, especially among immunocompromised individuals. The rise of multidrug resistant strains of A. baumannii has limited the use of standard antibiotics, highlighting a need for new drugs that exploit novel mechanisms of pathogenicity. Disrupting iron acquisition by inhibiting the biosynthesis of iron-chelating molecules (siderophores) secreted by the pathogen is a potential strategy for developing new antibiotics. Here we investigated FbsI, an N-hydroxylating monooxygenase involved in the biosynthesis of fimsbactin A, the major siderophore produced by A. baumannii. FbsI was characterized using steady-state and transient-state



kinetics, spectroscopy, X-ray crystallography, and small-angle X-ray scattering. FbsI was found to catalyze the *N*-hydroxylation of the aliphatic diamines putrescine and cadaverine. Maximum coupling of the reductive and oxidative half-reactions occurs with putrescine, suggesting it is the preferred (*in vivo*) substrate. FbsI uses both NADPH and NADH as the reducing cofactor with a slight preference for NADPH. The crystal structure of FbsI complexed with NADP⁺ was determined at 2.2 Å resolution. The structure exhibits the protein fold characteristic of Class B flavin-dependent monooxygenases. FbsI is most similar in 3D structure to the cadaverine *N*-hydroxylases DesB and DfoA. Small-angle X-ray scattering shows that FbsI forms a tetramer in solution like the *N*-hydroxylating monooxygenases of the SidA/IucD/PvdA family. A model of putrescine docked into the active site provides insight into substrate recognition. A mechanism for the catalytic cycle is proposed where dehydration of the C4a-hydroxyflavin intermediate is partially rate-limiting, and the hydroxylated putrescine product is released before NADP⁺.

A cinetobacter baumannii is a Gram-negative opportunistic pathogen that is responsible for nosocomial infections, especially among immunocompromised individuals. ¹ A. baumannii is responsible for nearly 20% of intensive care unit infections worldwide. ² The bacteria is responsible for infections in the bloodstream, respiratory system, urinary tract, and soft tissues. ³ Treatment of A. baumannii infections usually consists of administration of β-lactam antibiotics; however, the rise of multidrug resistant strains has limited the use of these and other antibiotics against this bacterium. ^{4,5}

One of the primary virulence factors associated with *A. baumannii* infection are siderophores. Siderophores are ferric iron-chelating compounds found in bacteria and fungi that scavenge free iron from the host, which is then used for microbial pathogen growth and virulence. *A. baumannii* produces three structurally unique siderophores: acinetobactin, baumannoferrin, and fimsbactin. Acinetobactin is the best characterized siderophore and is present in nearly all clinical isolates of *A. baumannii*. The baumannoferrins are another siderophore released by *A. baumannii* and are the most recently identified. The structure of baumannoferrin contains a hydroxamate moiety and a large hydrophobic region, which has been hypothesized to be associated with membrane

associated iron transport.¹⁰ The fimsbactins were first identified in the clinical isolate *A. baumannii* ATCC 17978.⁹ Genomic analysis revealed a conserved biosynthetic operon that encodes all the enzymes required for production of hydroxamate-containing fimsbactins A–F.¹¹ Fimsbactin A is the major siderophore produced and is directly implicated in iron uptake, while B–F are believed to transport biosynthetic intermediates involved in siderophore biosynthesis.⁹ The production of three distinct classes of siderophores by *A. baumannii* is not uncommon; the production of multiple siderophores is associated with competition among pathogenic microbes in nutrient-limiting conditions.^{12–15}

The fimsbactin A biosynthetic gene cluster encodes a nonribosomal peptide synthase (NRPS), regulatory proteins, and tailoring enzymes involved in the synthesis of the 2,3-

Received: August 25, 2022 Revised: October 7, 2022 Published: October 31, 2022





dihydroxybenzovl and N-acetyl-N-hydroxyputrescine moieties of the siderophore. One essential fimsbactin A biosynthetic enzyme, FbsI, has been annotated as a member of the SidA/ IucD/PvdA family of monooxygenases and is thus predicted to be an NADPH-dependent N-hydroxylating monooxygenase (NMO) (EC 1.14.13.59). NMOs belong to the larger family of flavoproteins known as flavin-dependent monooxygenases (FMOs). FMOs are characterized by using a bound flavin prosthetic group, either FMN or FAD, to perform unique oxidation reactions following flavin reduction. 17 Analysis of FbsI's amino acid sequence shows that it likely belongs to the Class B FMOs, which oxygenate small heteroatomic substrates and have two Rossmann-fold nucleotide binding domainsone for FAD/FMN and the other for the NADPH/NADH reducing cofactor. FbsI is the first of three enzymes involved in producing the hydroxamate moiety of fimsbactin A. FbsI is hypothesized to catalyze the N-hydroxylation of the aliphatic diamine putrescine into N-hydroxyputrescine (NHP) (Figure 1A). N-Acetyl-NHP is then produced by the enzymes FbsJ and

Figure 1. (A) Reaction catalyzed by FbsI. (B) Structure of fimsbactin A, a primary siderophore produced by *A. baumannii*.

Fimsbactin A

FbsK. Lastly, the *N*-acetyl-NHP moiety is added to the fimsbactin scaffold synthesized by the NRPS to produce functional fimsbactin A (Figure 1B). Knockout of the *fbsI* gene shows that the NHP moiety is not produced, suggesting its specific hydroxylation activity.⁹ In this work, we report the production of recombinant FbsI, the steady-state and transient-state kinetic characterization, the crystal structure of flavin-bound FbsI in complex with NADP⁺, and determination of the oligomeric structure in solution from small-angle X-ray scattering (SAXS).

EXPERIMENTAL PROCEDURES

Protein Production and Purification. The FbsI gene subcloned into the pET28a expression vector was provided by Jinping Yang and Dr. Timothy Wencewicz (Washington University in St. Louis). pET28afbsI was transformed into OneShot BL21 (DE3) *Escherichia coli* cells purchased from Thermo Fisher Scientific (Waltham, MA). Overnight cultures were made by inoculating 50 mL of Luria–Bertani (LB) medium (10 g tryptone, 10 g sodium chloride, 5 g yeast extract per liter) supplemented with kanamycin (25 μ g/mL) with a single colony of transformed *E. coli* cells and incubated for 12 h

at 37 °C with agitation at 250 rpm. For FbsI expression, 8 mL of overnight culture was used to inoculate 1 L of LB medium supplemented with kanamycin (50 $\mu g/mL$). Cultures were grown at 37 °C with agitation at 250 rpm until reaching an OD₆₀₀ of 0.8, where 0.5 mM isopropyl β -D-thiogalactopyranoside (IPTG) was added to induce expression of FbsI. The temperature was lowered to 18 °C, and cultures were allowed to continue growing for 16 h. Cells were harvested by centrifugation at 4000g at 4 °C for 20 min and immediately stored at -70 °C.

Cells were resuspended (5 mL buffer/g cells) in Buffer A (25 mM HEPES, 300 mM NaCl, 20 mM imidazole, 10% glycerol, pH 7.5) supplemented with 1 mg/mL DNase, 1 mg/ mL RNase, 1 mg/mL lysozyme, and 1 mM phenylmethylsulfonyl fluoride (PMSF) and were continuously stirred at 4 °C for 30 min. The resuspended cells were lysed using sonication (Fisher Scientific Model 500) at 70% amplitude with cycles of 5 s on and 10 s off for 15 min. Cell debris was removed by centrifugation at 24 000g at 4 °C for 45 min. The clarified supernatant was loaded onto two in-tandem 5 mL HisTrap FF nickel IMAC columns equilibrated in three column volumes of Buffer A using an AKTA Start FPLC (GE Healthcare, Chicago, IL). Following protein loading, the columns were washed with approximately 50 mL of Wash Buffer (25 mM HEPES, 300 mM NaCl, 30 mM imidazole, 10% glycerol, pH 7.5). FbsI was eluted with Buffer B (25 mM HEPES, 300 mM NaCl, 500 mM imidazole, 10% glycerol, pH 7.5) using a linear gradient method. Yellow fractions, indicative of flavin-bound protein, were pooled together and dialyzed overnight into Buffer C (25 mM HEPES, 150 mM NaCl, 10% glycerol, 1 mM TCEP, pH 7.5). The dialyzed protein solution was concentrated using a 30 kDa centrifuge filter (Sigma-Aldrich, St. Louis, MO) and flash-frozen with liquid nitrogen before being stored at -70 °C. Purity of purified FbsI was evaluated using a 12% acrylamide SDS-PAGE analysis. The extinction coefficient for FbsI based on FAD concentration was determined as described previously. 18,19

Oxygen Consumption Assay. The consumption of oxygen by FbsI was measured using an oxygen electrode system (Hansatech, Norfolk, England). Steady-state kinetic parameters were determined by varying concentrations of substrate or NAD(P)H at a constant FbsI concentration (1 μM). All assays were performed in 25 mM HEPES, pH 7.5, at a volume of 1 mL. Reaction components were continuously stirred and incubated for at least 30 s before initiating with NAD(P)H. All oxygen consumption assays were performed at room temperature (22 ± 2 °C). Data that showed a rectangular hyperbola were fit to eq 1, while data following substrate inhibition kinetics were fit to eq 2. The k_{cat} is the turnover number, [S] is substrate concentration, [E] is FbsI concentration, $K_{\rm m}$ is the Michaelis constant, and $K_{\rm i}$ is the inhibitor constant. All graph fitting analysis was performed using Kaleidagraph (Synergy Software, Reading, PA).

$$\frac{\nu_{\rm o}}{[E]} = \frac{k_{\rm cat}[S]}{K_{\rm m} + [S]} \tag{1}$$

$$\frac{v_{\rm o}}{[E]} = \frac{k_{\rm cat}[S]}{K_{\rm m} + [S] + \frac{[S]^2}{K_{\rm i}}}$$
(2)

Product Formation Assay. The amount of hydroxylated amine products produced by FbsI was measured using a modified Csaky iodine oxidation assay.^{20–22} Reaction mixtures

consisted of 1 µM FbsI, 500 µM NADPH, varied substrate concentrations (2.5–2000 μ M), and 25 mM HEPES, pH 7.5, in a final reaction volume of 120 μ L. Standard solutions of varied hydroxylamine concentrations (0-300 μ M) were also prepared. Reactions were initiated by addition of NADPH and were allowed to incubate at room temperature, with continuous shaking, for 5 min. Reactions were quenched by the addition of 62.4 μ L 2 N perchloric acid and centrifuged at 16 000 rpm for 2 min. A 47 μ L aliquot of each reaction's supernatant was transferred, in triplicate, to a 96-well plate. Equal volumes (47 μ L) of 10% w/v sodium acetate and 1% w/ v sulfanilic acid in 25% glacial acetic acid were added to the reactions. 0.5% w/v iodine in 100% glacial acetic acid (19 μ L) was added, and reactions were incubated in the dark for 15 min. Color development was initiated by adding equal volumes (19 μ L) of 0.1 N sodium thiosulfate and 0.6% w/v 1naphthylamine. After shaking for 45 min, assay plates were read at 562 nm using a Molecular Devices SpectraMax M5 plate reader.

Detection of Products via Liquid Chromatography-Mass Spectrometry (LC-MS) Analysis. Reaction assays (300 μ L) consisting of 25 mM HEPES, pH 7.5, 25 μ M putrescine, 500 µM NADPH, and 1 µM FbsI were incubated at room temperature. After 10 min, aliquots (50 μ L) were quenched with acetonitrile (100 μ L) and chilled at -20 °C for 10 min. Following centrifugation at 16 000 rpm for 1 min, the supernatant was added to 50 μ L of 100 mM borate buffer, pH 8.0, followed by 20 μ L of 10 mM fluorenylmethyloxycarbonyl (Fmoc)-Cl dissolved in HPLC-grade methanol. Following derivatization for 5 min, 20 µL of 100 mM 1-adamantylamine (ADAM) dissolved in 1:1 0.2 mM HCl:MeCN was added to the reaction and allowed to incubate at room temperature for 15 min to remove excess Fmoc-Cl. Samples were then analyzed on a Waters Synapt Q-TOF mass spectrometer interfaced with a Waters Acquity UPLC (Waters Corp, Milford Ma.) The UPLC was operated at a flow rate of 0.2 mL/min, and 10 μ L of sample was injected onto a Waters Acquity BEH C18 column (Waters Corp., Milford, MA) maintained at 35 °C. The mobile phase consisted of A (water (Thermo Fisher Scientific, Waltham, MA) + 0.1% formic acid (Sigma-Aldrich, St. Louis, MO)) and B (acetonitrile (Thermo Fisher Scientific, Waltham, MA) + 0.1% formic acid). A binary gradient was used from 0 to 10 min at the following conditions: 0-1 min 10% B, linear gradient to 90% B at 8 min, 8.5 min return to initial conditions. The mass spectrometer was operated in positive ion mode with electrospray ionization. The mass range was $100-1400 \ m/z$, and the source conditions were set to capillary voltage 3.0 V, cone voltage 30 V, source offset 80, source temperature 125 °C, desolvation temperature 400 °C, cone gas 50 L/h, desolvation gas 500 L/h, and nebulizer 6 bar. Data were collected in MSe mode with a 0.2 s cycle time and a collision energy ramp at 20-45 V in the high energy function. Leucine enkephalin was infused at 5 μ L/min for mass correction at 20 s intervals with a 0.2 s cycle time. The data was analyzed with Mass Lynx (V 4.1, Waters Corp., Milford MA).

NADP⁺ **Inhibition.** The effects of NADP⁺ on FbsI activity were measured using the oxygen consumption assay. All reactions consisted of 1 μ M FbsI, 25 μ M putrescine, 0–1000 μ M NADPH, and 25 mM HEPES, pH 7.5. NADP⁺ concentrations were varied at 0, 250, 500, and 1000 μ M. Inhibition constants were calculated by plotting the data as double-reciprocal plots.

Size-Exclusion Chromatography. A 750 μ L sample of 5 mg/mL FbsI was injected onto a HiPrep 16/60 Sephacryl S-200 HR column equipped to an AKTA Prime Plus (GE Healthcare, Chicago, IL). The column was equilibrated in Gel Filtration Buffer (50 mM potassium phosphate, 150 mM NaCl, pH 7.5) at a flow rate of 1.0 mL/min. To quantify the oligomeric state of FbsI, a standard curve was produced using a high-molecular-weight gel filtration calibration kit (GE Healthcare, Chicago, IL) along with His⁶-TEV protease and RNase (Sigma-Aldrich, St. Louis, MO). The standard curve contained ferritin (440 kDa), aldolase (158 kDa), conalbumin (75 kDa), His⁶-TEV protease (27 kDa), and RNase (13 kDa). Blue dextran (~2000 kDa) was used to calculate the void volume of the column. Fractions containing FbsI were confirmed by using SDS-PAGE analysis.

Stopped-Flow Spectrophotometry. All stopped-flow assays were performed with a SX20 stopped-flow spectrophotometer equipped with a photodiode array detector (Applied Photophysics, Surrey, UK) housed inside an anaerobic glovebox (COY Laboratories, Grass Lake, MI). Prior to performing assays, the sample-handling unit of the instrument was made anaerobic by scrubbing oxygen with a mixture of dextrose (Thermo Fisher Scientific, Waltham, MA) and glucose oxidase (Sigma-Aldrich, St. Louis, MO) from Aspergillus niger. Buffer solutions were made anaerobic using a Schlenk line apparatus as described previously.²³ In short, solutions sealed in Büchner flasks were deoxygenated with four cycles of high vacuum pressure (4 min) and ultrapure argon (1 min). FbsI samples were deoxygenated with 15 cycles of high vacuum pressure (2 s) and ultrapure argon (4 s). NAD(P)H and putrescine were prepared by dissolving in anaerobic 25 mM HEPES, pH 7.5 buffer. All stopped-flow experiments were performed at room temperature (22 \pm 2 °C).

For the reductive half-reaction, 17 μ M FbsI was mixed with 62.5–2000 μ M NADPH or NADH using the single mixing mode. For assays in the presence of substrate, 25 μ M putrescine was incubated with FbsI prior to mixing with NADPH. Spectra from 190–800 nm were collected on a logarithmic scale for 100 s (NADPH) or 250 s (NADH). Traces at 450 nm were fit with a double-exponential decay equation (eq 3). For eq 3, a_1 is the amplitude for the first defined phase, $k_{\rm obs1}$ is the observed reaction rate of the first phase, a_2 is the amplitude for the second phase, $k_{\rm obs2}$ is the observed reaction rate of the second phase, t is the assay time, and t0 is the final absorbance.

Abs =
$$a_1 e^{-k_{\text{obs}_1}t} + a_2 e^{-k_{\text{obs}_2}t} + C$$
 (3)

For the oxidative half-reaction, 17 µM FbsI was first mixed with 34 μ M anaerobic NADPH to fully reduce the enzyme. Oxygen saturated buffer was prepared by flushing with pure oxygen gas for 1 h at 0 °C with constant stirring, creating a 1.2 mM dissolved O₂ concentration in the buffer. Using the single mixing mode, reduced enzyme was mixed with 25-600 μ M oxygen for 500 s (no putrescine) or 250 s (with putrescine). Traces at 370 and 450 nm were fit with either a singleexponential rise equation (eq 4) or a double-exponential rise equation (eq 5). For eq 4, a is the amplitude, $k_{\rm obs}$ is the observed reaction rate, t is the assay time, and D is the initial absorbance. For eq 5, a_1 is the amplitude for the first phase, $k_{\rm obs1}$ is the observed reaction rate of the first phase, a_2 is the amplitude for the second phase, $k_{\rm obs2}$ is the observed reaction rate of the second phase, t is the assay time, and D is the final absorbance.

$$Abs = a(1 - e^{-k_{obs}t}) + D$$
(4)

Abs =
$$a_1(1 - e^{-k_{obs_1}t}) + a_2(1 - e^{-k_{obs_2}t}) + D$$
 (5)

Crystallization. Initial screening of FbsI using Crystal Screen 1 and 2 kits and the Index kit (Hampton Research) was done with 6.5 and 12 mg/mL FbsI in the presence of 5 mM NADP⁺. A drop ratio of 1:1 protein:screening solution was used. Small, yellow crystals formed in a condition containing 0.05 M ammonium sulfate, 0.05 M Bis-Tris pH 6.5, and 30% pentaerythritol ethoxylate (15/4 EO/OH). The crystals were cryoprotected by creating a mixture of 80% reservoir solution and 20% PEG 200 by taking 8 μ L of the screening condition from the reservoir and adding 2 μ L of 100% PEG 200. This solution was added to the crystals, and after a minute, the crystals were flash-cooled in liquid nitrogen.

X-ray Crystal Structure Determination. X-ray diffraction data from a crystal of the NADP⁺ complex were collected at Advanced Photon Source beamline 24-ID-E using an Eiger-16 M detector. The data were processed with XDS²⁴ and AIMLESS.²⁵ The space group is $P2_1$ 2_1 with the unit cell dimensions listed in Table 1. Analysis of solvent content suggested the asymmetric unit contains four FbsI chains with a Matthews coefficient of 2.7 Å³/Da and 54% solvent content.²⁶ Data processing statistics are summarized in Table 1.

Initial phases for the FbsI-NADP+ complex were calculated using molecular replacement. A monomer search model was generated from the structure of Streptomyces sviceus DesB in complex with NADP⁺ (PDB ID 6XBB)²⁷ with Chainsaw²⁸ using the C γ -truncation option. FbsI and SsDesB are 47% identical in amino acid sequence. Molecular replacement calculations were performed with Phaser as implemented in Phenix. 29,30 Phaser identified a solution having four molecules arranged as a tetramer with D2 symmetry. The structure from Phaser was completed through several cycles of iterative modeling in Coot³¹ and refinement in Phenix. The ligands FAD and NADP+ were refined with occupancy fixed at 1.0. PEG fragments were modeled near the ε -amino group of Lys188. The structure was validated using polder omit maps,³² MolProbity,³³ and the PDB validation server.³⁴ Refinement statistics are listed in Table 1. Coordinates and structure factor amplitudes have been deposited in the PDB under accession code 7US3.

Small-Angle X-ray Scattering (SAXS). A sample of FbsI at 12 mg/mL was dialyzed against a buffer consisting of 25 mM HEPES, pH 7.5, 150 mM NaCl, and 1 mM TCEP. The dialyzed sample was pipetted into a 96-well tray at nominal concentrations in the range of 1-9 mg/mL. The dialysate was reserved for measurement of the background SAXS curve. Shutterless SAXS data collection was performed at 20 °C using a Pilatus detector at beamline 12.3.1 of the Advanced Light Source through the SIBYLS Mail-in High Throughput SAXS program.³⁵ The total exposure time was 10 s per sample, framed every 0.33 s (30 frames total). The wavelength was 1.234 Å. Buffer-subtracted SAXS curves were averaged using SAXS FrameSlice. PRIMUS³⁶ was used to perform Guinier analysis, calculate the distance distribution function, and estimate the molecular mass. The molecular mass was also estimated using the SAXSMoW server.³⁷ Theoretical SAXS curves were calculated using FoXS.³⁸ Models of the tetramer including residues not observed in the crystal structure were generated with AllosMod-FoXS using the default (most conservative) settings. The SAXS data, P(r) curves, and best

Table 1. X-ray Diffraction Data Collection and Refinement Statistics

	Space group	$P \ 2_1 \ 2_1 \ 2_1$
τ	Unit cell parameters (Å)	a = 124.83
		b = 126.31
		c = 140.25
7	Wavelength (Å)	0.97918
I	Resolution (Å)	140.25-2.20 (2.24-2.20)
(Observations ^a	902459 (32196)
τ	Unique reflections ^a	111523 (4908)
1	$R_{\text{merge}}(I)^a$	0.235 (1.383)
	$R_{\text{meas}}(I)^a$	0.268 (1.502)
	$R_{\text{pim}}(I)^a$	0.095 (0.570)
	Mean I/σ^a	8.8 (1.3)
($CC_{1/2}^{a}$	0.987 (0.466)
(Completeness (%) ^a	99.3 (89.0)
1	Multiplicity ^a	8.1 (6.6)
1	No. of protein residues	1712
1	No. of atoms	
I	Protein	13 754
I	FAD	212
1	NADP ⁺	192
7	Water	603
1	R _{cryst} a	0.1817 (0.3064)
1	R _{free}	0.2225 (0.3268)
	RMSD bonds (Å)	0.007
I	RMSD angle (deg)	0.890
I	Ramachandran plot c	
I	Favored (%)	96.65
(Outliers (%)	0.12
(Clashscore (PR) ^c	3.17 (99)
1	MolProbity Score (PR) ^c	1.73 (95)
I	Average B-factor (Ų)	
I	Protein	38.6
I	FAD	36.9
1	NADP ⁺	41.7
7	Water	36.9
I	PDB ID	7US3

^aValues for the outer resolution shell of data are given in parentheses. ^b5% test set. ^cFrom MolProbity. The percentile ranks (PR) for Clashscore and MolProbity score are given in parentheses.

fit models have been deposited in the SASBDB under the accession codes listed in Table $4.^{39}$

RESULTS

Expression, Purification, and Solution Molecular Weight. Recombinant FbsI was subcloned into the pET28a vector and expressed with an N-terminus His6 affinity tag in E. coli BL21 (DE3) cells. The resuspended cell pellet was purified using Ni-NTA immobilized metal affinity chromatography (IMAC). Yellow fractions, indicative of flavin-bound protein, were collected and analyzed using SDS-PAGE, showing FbsI was purified at >95% homogeneity (Figure S1A). The protein yield for FbsI was 18 mg protein/liter of bacterial culture. The UV-visible absorbance spectrum of FbsI showed two characteristic peaks at 370 and 450 nm, further indicative of FAD bound protein (Figure S1B). The extinction coefficient for FbsI based on FAD concentration at pH 7.5 was determined to be 12.99 mM⁻¹ cm⁻¹. The native molecular weight of FbsI in solution was estimated using size-exclusion chromatography. A standard curve was used to estimate a

Table 2. Steady-State Kinetic Parameters of FbsI Determined by the Oxygen Consumption and Product Formation Assays

Variable Substrate ^a	Fixed Substrate	$K_{\mathrm{m}}~(\mu\mathrm{M})$	$k_{\rm cat}~({\rm s}^{-1})$	$k_{\rm cat}/K_{\rm m}~({ m M}^{-1}~{ m s}^{-1})$	$K_{\rm i}~(\mu{ m M})$			
Oxygen consumption								
Putrescine	NADPH	3.0 ± 2.0	0.60 ± 0.10	208000 ± 33000	120 ± 50			
Cadaverine	NADPH	9.0 ± 2.0	0.54 ± 0.20	58000 ± 11000	220 ± 70			
NADPH	Putrescine	60 ± 10	0.70 ± 0.04	11400 ± 2500	-			
NADH	Putrescine	55 ± 20	0.30 ± 0.10	5000 ± 400	-			
Product formation assay								
Putrescine	NADPH	6.0 ± 2.0	0.65 ± 0.04	102000 ± 27000	1900 ± 500			
Cadaverine	NADPH	8.0 ± 0.70	0.12 ± 0.06	14300 ± 820	-			
NADPH	Putrescine	58 ± 14	0.70 ± 0.10	12000 ± 1000	-			
NADH	Putrescine	200 ± 90	0.37 ± 0.062	1850 ± 650	-			

^aFixed concentrations were at 0.5 mM NADPH or 0.025 mM putrescine.

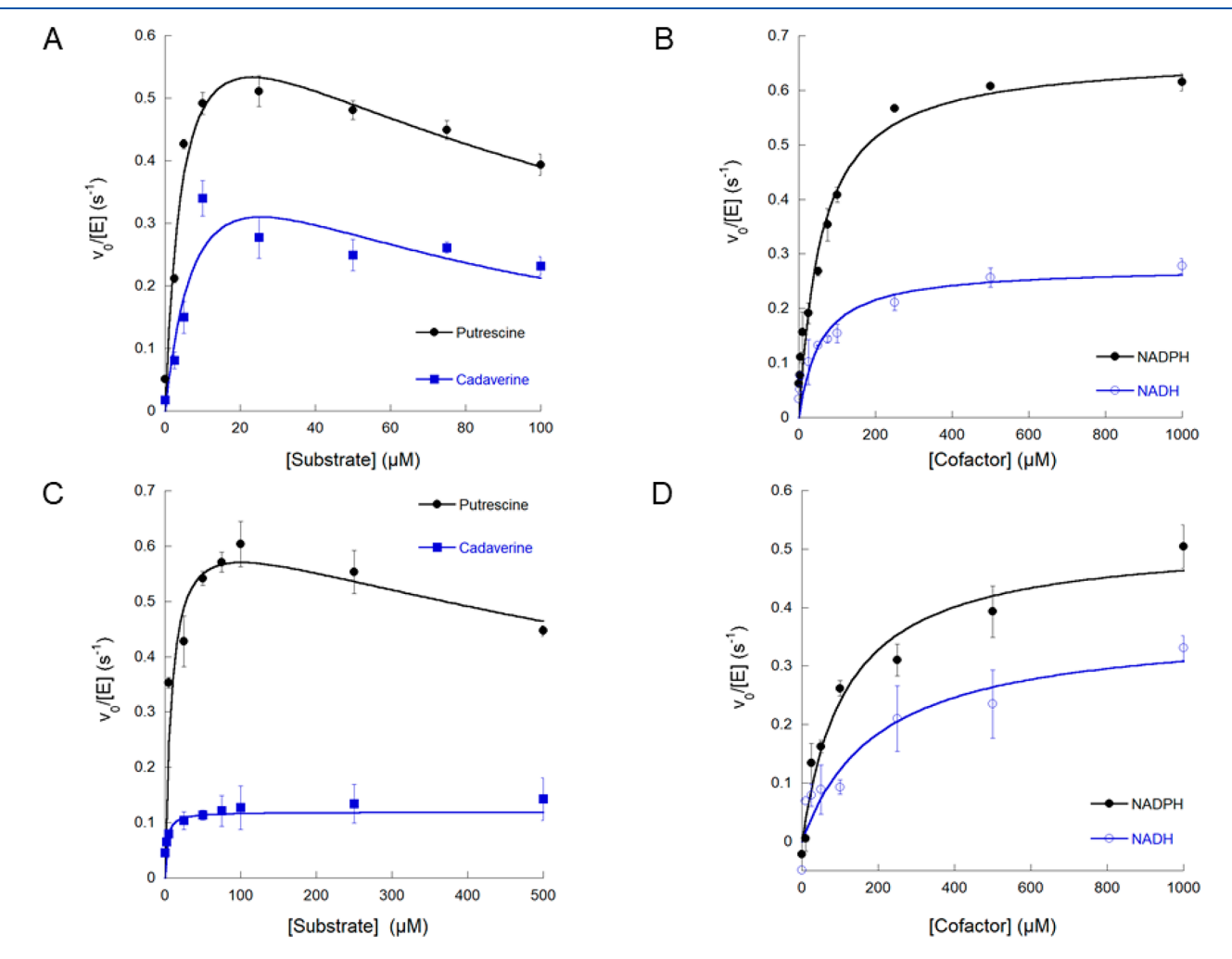


Figure 2. Steady-state kinetic analysis of FbsI. (A) Measurement of initial rate conditions when varying putrescine (black circle) and cadaverine (blue square) concentrations and (B) NADPH (black solid circle) and NADH (blue open circle) concentrations using the oxygen consumption assay. (C) Measurement of initial rate conditions when varying putrescine (black circle) and cadaverine (blue square) concentrations and (D) NADPH (black solid circle) and NADH (blue open circle) concentrations using the hydroxylated amine product formation assay.

molecular weight of FbsI in solution of \sim 248 000 Da, consistent with FbsI forming a tetramer in solution (monomer MW = 53 500 Da) (Figure S2).

Steady-State Kinetic Analysis. The steady-state kinetic parameters for FbsI were determined using an oxygen consumption assay. All assays were performed using 25 mM HEPES, pH 7.5, and an enzyme concentration of 1 μ M. For the oxygen consumption assay, substrate selectivity of FbsI was determined by varying concentrations of putrescine, cadaver-

ine, L-ornithine, and L-lysine. The enzyme showed the greatest activity with putrescine, with an apparent $K_{\rm m}$ of 3.0 \pm 2.0 μ M and a $k_{\rm cat}/K_{\rm m}$ of 208 000 \pm 30 000 M $^{-1}$ s $^{-1}$ (Table 2). FbsI showed a nearly 4-fold reduction in the catalytic efficiency with cadaverine when compared to putrescine (Figure 2A). No significant changes in activity were detected when varying L-lysine and L-ornithine concentrations, as the estimated $k_{\rm obs}$ of \sim 0.1 s $^{-1}$ for these compounds is equivalent to background NADPH oxidation (not shown). Preference for the reducing

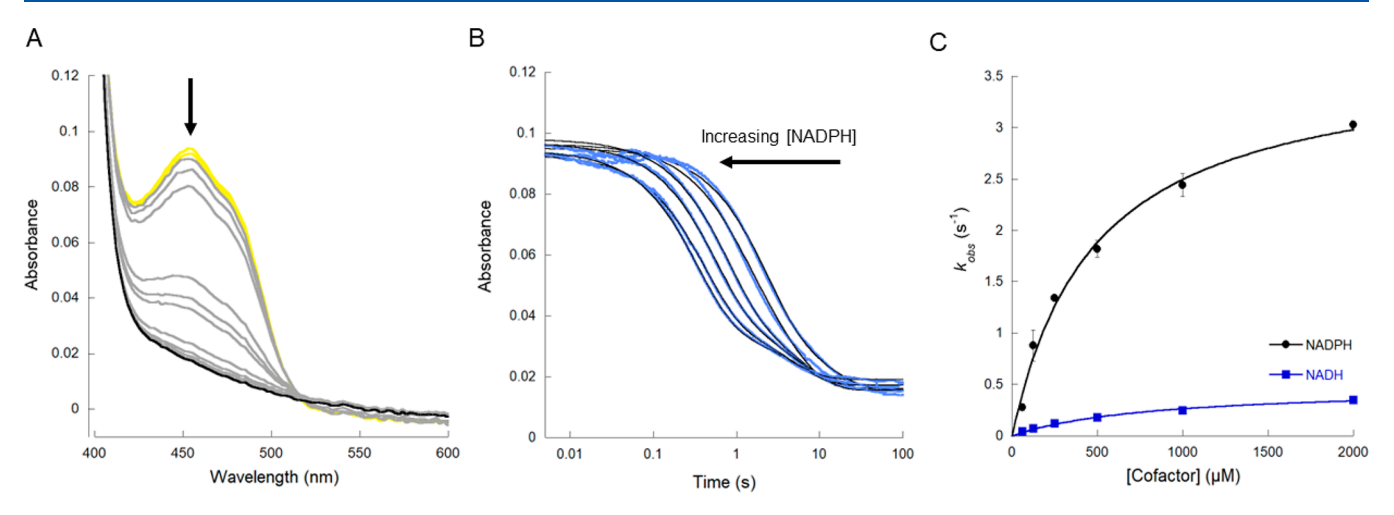


Figure 3. Measuring flavin reduction using stopped-flow spectroscopy. (A) Bleaching of the peak at 450 nm over 100 s following reduction of FbsI with 2 mM NADPH. The yellow line represents fully oxidized flavin, while the black line represents reduced flavin. (B) Traces at 450 nm when titrating with increasing concentrations of NADPH over 100 s. Traces were fit with eq 3, as shown by the solid black line. (C) Measurement of rapid-reaction rate constants when titrating increasing concentrations of NADPH (black circle) and NADH (blue square) against oxidized FbsI.

cofactors NADH and NADPH was also measured (Figure 2B). The $K_{\rm m}$ values for NADH and NADPH are nearly identical; however, the $k_{\rm cat}$ is ~2.3-fold faster with NADPH compared to NADH (Table 2). The effect of various concentrations of NADP⁺ on the kinetic parameters was measured to determine the mode of inhibition by NADP⁺. The double-reciprocal plot analysis shows that the lines have different slopes and the same *y*-intercept, consistent with NADP⁺ being a competitive inhibitor against NADPH (Figure S3).

The steady-state kinetic parameters were also measured by monitoring formation of the product N-hydroxyputrescine using a modified Csaky iodine oxidation assay. Putrescine and cadaverine concentrations were varied the same as with the oxygen consumption assay (Figure 2C). The k_{cat}/K_{m} when varying putrescine was over 7-fold faster than when varying cadaverine (Table 2). No product formation was observed when varying L-lysine or L-ornithine concentrations (not shown). When varying reducing cofactor concentration, the k_{cat} for NADPH was ~2-fold higher than that of NADH, and the $K_{\rm m}$ of NADPH was ~4-fold lower than that of NADH (Figure 2D, Table 2). The latter trend was not observed with the oxygen consumption assay, where the $K_{\rm m}$ values for the two reducing cofactors were nearly identical (Table 2). This difference is likely due to the production of H₂O₂ by FbsI, a process known as uncoupling. The coupling efficiency, taken as a ratio of k_{cat} between the iodine oxidation and oxygen consumption assays, for putrescine is $108 \pm 4\%$ compared to $22 \pm 3\%$ for cadaverine, suggesting that uncoupling occurs when cadaverine is present. These results suggest that putrescine is the preferred substrate.

Detection of N-Hydroxyputrescine. To further confirm that putrescine is being hydroxylated by FbsI to form *N*-hydroxyputrescine, LC-MS was utilized. Reactions containing putrescine along with controls without NADPH or FbsI present were derivatized using Fmoc-Cl and submitted for LC-MS analysis. All three reaction conditions had a peak with an m/z of 533.24 amu, corresponding to the structure of Fmocputrescine ($C_{34}H_{32}N_2O_4$). Only the reaction containing putrescine, NADPH, and FbsI contained a peak with an m/z of 549.24 amu, which is indicative of Fmoc-*N*-hydroxyputrescine ($C_{34}H_{32}N_2O_5$) (Figure S4).

Reductive Half-Reaction. Changes in flavin reduction for FbsI were measured using a stopped-flow spectrophotometer under anaerobic conditions. Bleaching of the prominent peak at 450 nm was observed when titrating oxidized FbsI with anaerobic NADPH and NADH (Figure 3A). The reduction process occurred with a fast and slow phase, with the fast phase representing $\sim 80\%$ of the absorbance changes. The slow and minor phase did not change as a function of NADPH concentrations and had a value of $\sim 0.2 \text{ s}^{-1}$. The rate constant for flavin reduction and binding affinities of the reducing cofactors are listed in Table 3. Increases in the $k_{\rm obs}$ (for the fast

Table 3. Rapid-Rate Kinetic Parameters for the Reductive Half-Reaction of FbsI

Variable Substrate	Fixed Substrate	$K_{\mathrm{D}}~(\mu\mathrm{M})$	$k_{\rm red}~({\rm s}^{-1})$
NADPH	-	500 ± 70	4.0 ± 0.20
NADPH	Putrescine	400 ± 100	3.0 ± 0.20
NADH	-	800 ± 100	0.50 ± 0.01

phase) were seen as increasing NADPH concentrations were tested (Figure 3B). A similar trend in reduction was also observed with NADH (data not shown). The rate of reduction ($k_{\rm red}$) of FbsI was nearly 8-fold faster with NADPH as the reducing cofactor compared to NADH (Figure 3C). Additionally, the $K_{\rm D}$ for NADH is approximately 1.6-fold higher than that of NADPH. The presence of putrescine does not significantly change the $K_{\rm D}$ value for NADPH, while the $k_{\rm red}$ only decreases by ~25%.

Oxidative Half-Reaction. Formation of the reactive C4a-hydroperoxyflavin intermediate along with flavin reoxidation was monitored using stopped-flow spectroscopy. Increases in the peaks at 370 and 450 nm were seen after titrating reduced FbsI with increasing concentrations of oxygen. In the absence of putrescine, an increase in the absorbance at 370 nm was observed (Figure 4A). This peak is consistent with the formation of the C4a-hydroperoxyflavin intermediate, where the rate constant for this process $(k_{\rm OOH})$ was $0.28 \pm 0.02~{\rm s}^{-1}$ at 250 μ M O₂. This was followed by an increase in absorbance at 450 nm, which corresponds to flavin oxidation via the release of hydrogen peroxide $(k_{\rm H2O2})$, with a maximum value of $0.02 \pm 0.004~{\rm s}^{-1}$ (Figure 4B). In the presence of

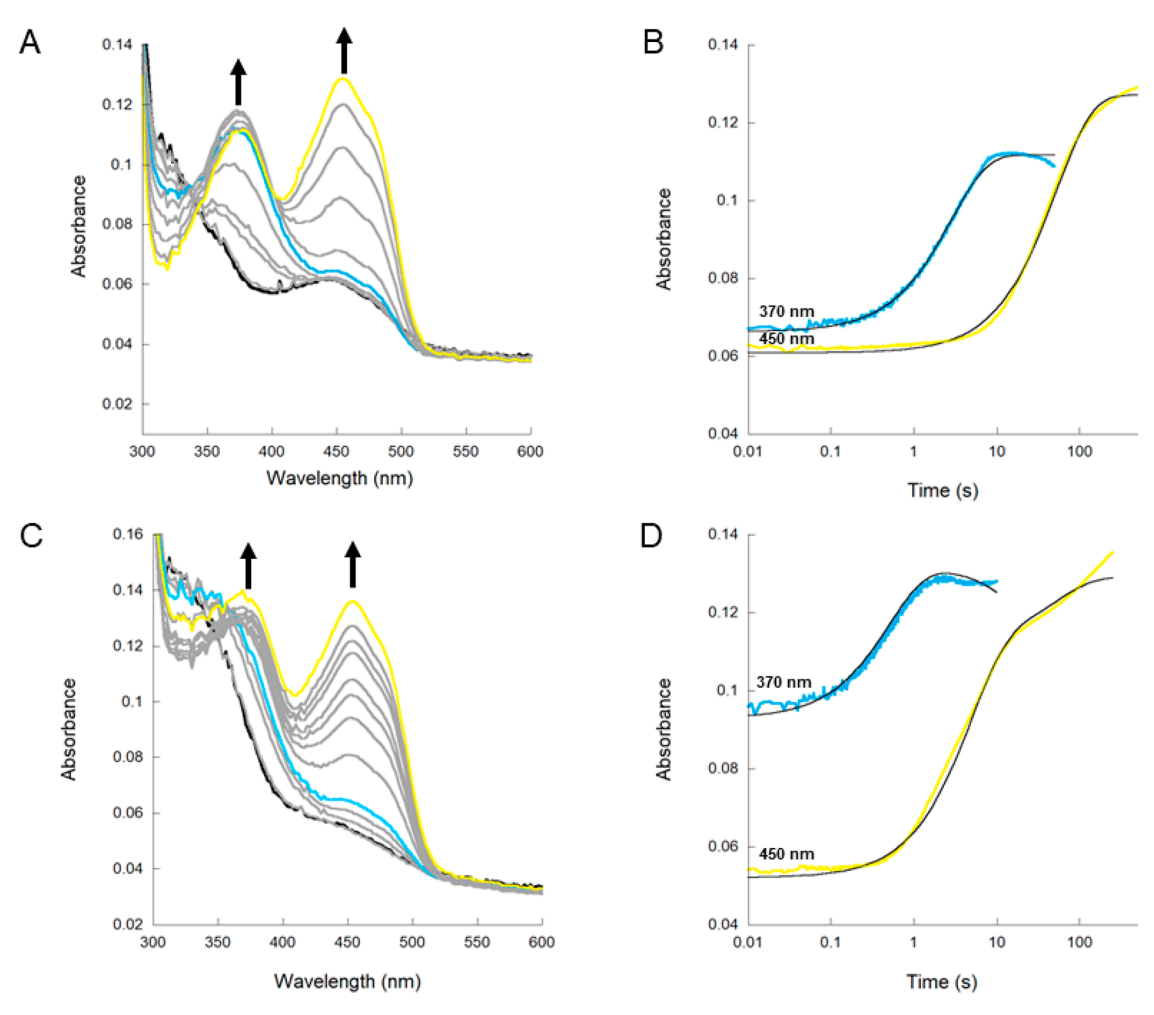


Figure 4. Measuring FbsI oxidation using stopped-flow spectroscopy. (A) Oxidation spectra of FbsI in the absence of putrescine at 250 μ M O₂ over 500 s. Arrows show the increase in absorbance at 370 and 450 nm over time. (B) Isolated traces at 370 nm (C4a-hydroperoxyflavin) and 450 nm (flavin reoxidation) in the absence of putrescine. Traces were fit with eq 4. (C) Oxidation spectra of FbsI in the presence of putrescine at 250 μ M O₂ over 250 s. (D) Isolated traces at 370 and 450 nm in the presence of putrescine. Traces were fit with eq 5.

putrescine, the C4a-hydroperoxyflavin peak formed much faster, as the $k_{\rm OOH}$ increased \sim 6-fold to 1.56 \pm 0.26 s⁻¹ at 250 μ M O₂ (Figure 4C). Because putrescine is hydroxylated by the C4a-hydroperoxyflavin intermediate, the increase in absorbance at 450 nm in the presence of putrescine represents flavin dehydration ($k_{\rm OH}$). This process of flavin oxidation occurred in two distinct phases, one fast (0.400 \pm 0.002 s⁻¹) and the other slow (0.030 \pm 0.003 s⁻¹) (Figure 4D).

Crystal Structure of Fbsl. The structure of FbsI complexed with NADP+ was determined at 2.20 Å resolution. Electron density supported the modeling of residues Gln4 through Val430 in all four polypeptide chains in the asymmetric unit without breaks (out of 466 total residues). FbsI exhibits the expected three-domain fold observed in other NMOs (Figure 5A). The two major domains each exhibit a Rossmann-like $\alpha/\beta/\beta$ three-layer sandwich. The N-terminal Rossmann-like domain binds FAD, while the C-terminal one binds NADP⁺. The FAD domain also supplies the amino acid substrate binding site. The smaller third domain consists of three α -helices (residues 70–114) and is involved in oligomerization (Figure 5A, right). The oligomerization domain contacts the amino acid substrate binding site, suggesting that oligomerization may be important for catalytic function.

The PDB was searched for structural neighbors of FbsI using PDBeFold. FbsI is most similar in both sequence and structure to the SsDesB and DfoA cadaverine N-hydroxylases (Table S1). FbsI is nearly 50% identical in sequence to these enzymes, and the structures align with a C- α RMSD of less than 1.0 Å (Figure S5A,B). FbsI shows lower similarity to ornithine and lysine N-hydroxylases. In this case, the sequence identity is less than 30%, and the RMSD is \sim 2.0 Å (Figure S5C,D). These results are consistent with the substrate of FbsI being more similar to cadaverine than either ornithine or lysine.

Oligomeric Structure of Fbsl. FbsI and its structural neighbors in the PDB (Table S1) all form a D_2 symmetry tetramer in the crystal (Figure 5B). In each case, the homotetramer is predicted to be stable in solution based on analysis of protein-protein interfaces using PDBePISA. We note that light scattering measurements suggested that PvdA is monomeric at 4.7 mg/mL. We are not aware of other biophysical characterizations of the oligomeric structures of NMOs. Thus, it is possible that PvdA, and potentially other related NMOs, exhibit a concentration-dependent self-association equilibrium in solution that favors the tetramer at the high protein concentrations used in crystallization. We

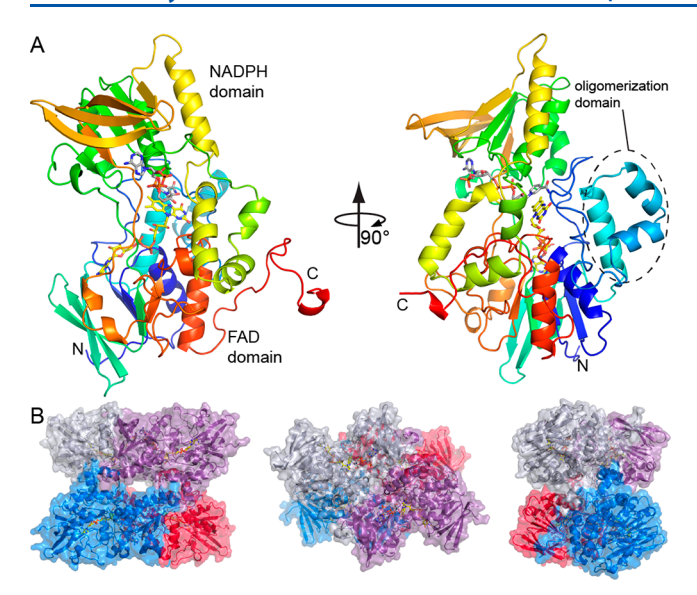


Figure 5. Fold and oligomeric structure of FbsI. (A) Protomer of FbsI complexed with FAD and NADP⁺. The protein is colored using a rainbow scheme with blue at the N-terminus and red at the C-terminus. FAD and NADP⁺ are shown in yellow and gray sticks, respectively. (B) The tetramer of FbsI viewed along its three mutually orthogonal twofold axes.

investigated this possibility for FbsI using small-angle X-ray scattering (SAXS).

The solution structural parameters of FbsI were determined from SAXS. SAXS data were collected at protein concentrations of 1-9 mg/mL (Table 4). The shape of the SAXS curve does not vary substantially with protein concentration (Figure 6A). In particular, the low-q region does not show evidence of concentration-dependent behavior, such as selfassociation (Figure 6B). The radius of gyration (R_{σ}) from both Guinier analysis (Figure 6C) and the pair distribution function (P(r)) is 41–42 Å (Table 4). For reference, the D_2 symmetry tetramer in the crystallographic asymmetric unit has an R_g of 36 Å. The P(r) curves are monomodal at all protein concentrations with a peak at r = 50-51 Å, consistent with the particle in solution having a compact, ellipsoidal shape (Figure 6D). The molecular weight from SAXS is 186-208 kDa based on Bayesian inference 46 and 218-231 kDa based on the SAXS MoW method³⁷ (Table 4). This range is within

 $2{-}13\%$ of the theoretical molecular weight of the FbsI tetramer (214 kDa), consistent with size-exclusion chromatography. Thus, the SAXS data are consistent with FbsI existing in solution as an ellipsoidal-shaped tetramer over the concentration range of 1–9 mg/mL. However, the discrepancy between the $R_{\rm g}$ from SAXS of 41–42 Å and that of the D_2 tetramer of only 36 Å suggests that the crystallographic D_2 tetramer does not fully account for the oligomeric structure of FbsI in solution.

The oligomeric structure of FbsI in solution was investigated further by calculating theoretical SAXS curves from models derived from the crystal structure. The curve calculated from the D_2 crystal tetramer shows reasonable overall agreement with the experimental data in that it accounts for the minimum near $q=0.104~{\rm \AA}^{-1}$ and the peak near $q=0.125~{\rm \AA}^{-1}$ (Figure 7A). The fit is poorer in the Guinier region, as expected given the 6 Å $R_{\rm g}$ mismatch.

We considered the possibility that the incompleteness of the crystal structure contributes to the suboptimal fit to the experimental SAXS profile. The crystal structure lacks 23 residues at the N-terminus and 15 residues at the C-terminus due to weak electron density. These disordered residues account for about 8% of the polypeptide chain. Schneidman-Duhovny et al. have stressed that modeling of a complete structure is critical for comparison of computed and experimental profiles.⁴⁷ The missing termini were modeled using AllosMod-FoXS⁴⁸ as extended polypeptide chains (Figure 7B), and their inclusion increased the R_g to 40 Å, which is within 1−2 Å of the SAXS value. The calculated SAXS profiles exhibit improved qualitative agreement with the experimental curves (Figure 7B) and substantially lower goodness-of-fit parameters (χ^2) for all six samples (Table 5). These are consistent with the D₂ tetramer being the predominant oligomeric structure of FbsI in solution.

We also considered the possibility that another tetrameric species—one with a larger $R_{\rm g}$ —is present in solution either alone or in equilibrium with the D₂ tetramer. Analysis of the protein-protein interfaces in the crystal with PDBePISA revealed an extended, asymmetric tetramer with an $R_{\rm g}$ of 46 Å (Figure 7C). The extended tetramer has very poor agreement with the experimental SAXS data (Figure 7C), as evidenced by χ^2 values of 2–35, compared to 0.1–1.1 for the complete D₂ tetramer (Table 5), indicating that this species does not predominate in solution. Modeling an ensemble of D₂

Table 4. Solution Structural Properties of FbsI from SAXS

Conc. (mg/mL)	1	3	5	6	8	9
Guinier analysis ^a						
$qR_{ m g}$ range	0.55-1.27	0.58 - 1.27	0.46 - 1.29	0.58 - 1.28	0.53-1.29	0.53 - 1.27
$R_{\rm g}$ (Å)	41.3 ± 1.2	41.3 ± 0.5	41.8 ± 0.5	41.6 ± 0.4	42.1 ± 0.4	42.3 ± 0.3
P(r) analysis ^a						
Points used	1-238	1-237	1-238	1-233	1-234	1-233
D_{max} (Å)	150	150	150	154	155	150
$R_{\rm g}$ (Å)	41.5	41.5	41.5	41.7	41.8	42.2
Porod Vol. (Å ³) ^a	394×10^{3}	395×10^{3}	391×10^{3}	392×10^{3}	394×10^{3}	397×10^{3}
MW (kDa)						
Bayesian Inf. ^{a,b}	185.8 (-13%)	185.8 (-13%)	185.8 (-13%)	208.0 (-3%)	208.0 (-3%)	185.8 (-13%)
SAXSMoW ^{c,b}	218.4 (+2%)	224.0 (+5%)	225.0 (+5%)	228.7 (+7%)	230.6 (+8%)	226.5 (+6%)
SASBDB	SASDNA9	SASDNB9	SASDNC9	SASDND9	SASDNE9	SASDNF9

 $[^]a$ Calculated with Primus. b The percent difference from the theoretical MW of the tetramer (214 kDa) is listed in parentheses. c Calculated with the SAXSMoW server

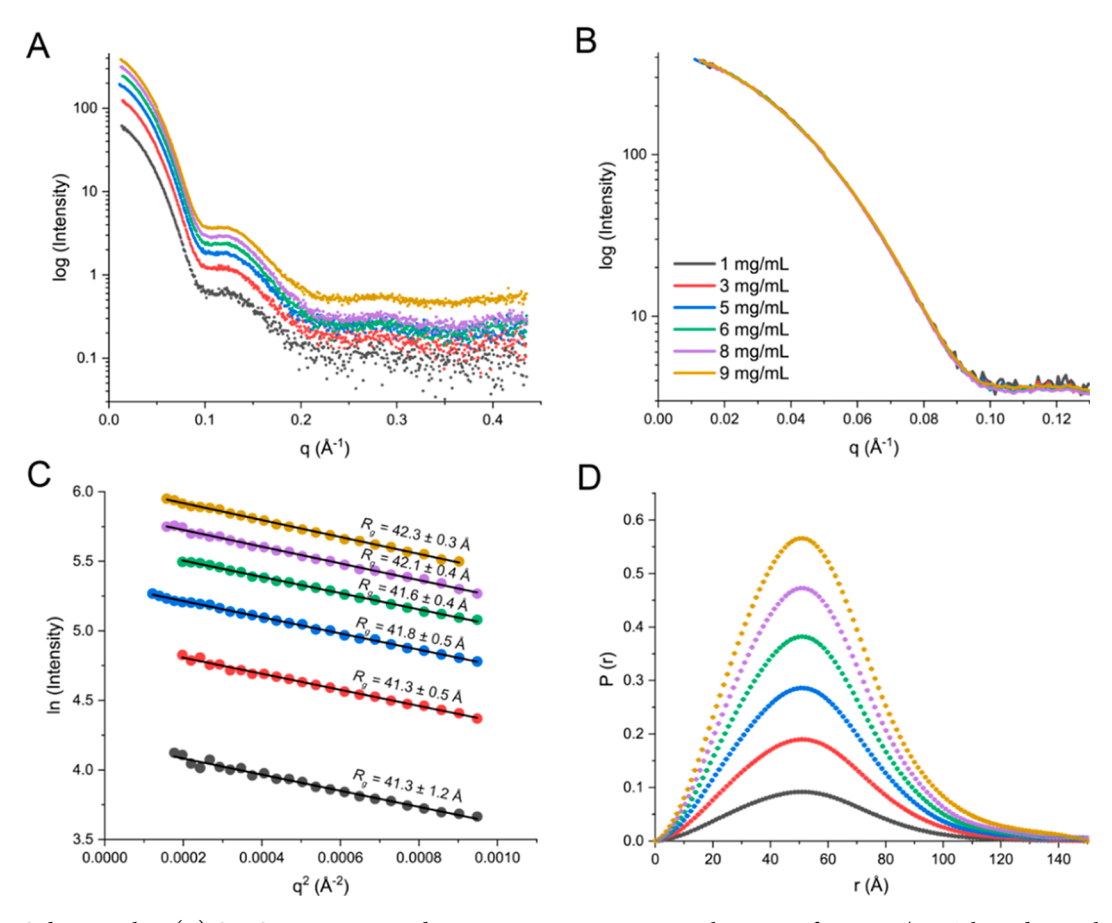


Figure 6. SAXS data on FbsI. (A) SAXS curves measured at protein concentrations in the range of 1–9 mg/mL. These data with uncertainties included are shown in Figure S7. (B) SAXS curves scaled for protein concentration highlighting the agreement at low q. (C) Guinier plots. (D) Distance distribution functions.

and extended tetramers using MultiFoXS did not improve the fits (i.e., MultiFoXS did not return a two-body result). These results suggest that the extended four-body assembly results from crystal packing and confirm that the D_2 tetramer is the predominant form of FbsI in solution.

Conformations and Interactions of FAD and NADP+. FbsI was cocrystallized with NADP+, and the electron density maps clearly indicated that both FAD and NADP+ were bound to the enzyme (Figure 8A). The conformations of these ligands were unambiguously defined by the electron density, except for the carboxamide of NADP+. The electron density for the carboxamide was somewhat variable, being the strongest in chains C and D (Figure S6) and weaker in chains A and B (Figure S6). The density in chains C and D was therefore used to determine the conformation of the carboxamide, within a dihedral rotation of 180°. The dihedral angle ambiguity was then resolved using hydrogen bonding. In particular, an atom of the carboxamide is within hydrogen bonding distance of the FAD O4 and N5 atoms. Since both FAD atoms are obligate hydrogen bond acceptors, the interacting atom of the carboxamide was assigned to be a hydrogen bond donor, i.e, the $-NH_2$ group (Figure S6).

The conformations of the FAD and NADP⁺ in FbsI are almost identical to those in the 2.37 Å resolution structure of cadaverine hydroxylase from *Streptomyces sviceus* (SsDesB). In both structures, the FAD adopts the "in" conformation, in which the *si*-face of the isoalloxazine is buried and the *re*-face is available to participate in catalysis (Figure 8B); this is the most common conformation observed in NMO structures.⁴⁹ The *si*-

face of the isoalloxazine in FbsI and SsDesB is braced by Leu, Trp, and His side chains, the latter two also hydrogen bonding to the FAD ribityl O4' (Figure 8B). The B side of the NADP+ nicotinamide packs against the re-face of the isoalloxazine; this is the same arrangement seen in the other NMO structures. The nicotinamide sits below an Arg-Glu ion pair and its carboxamide hydrogen bonds with the N5 edge of the FAD. Two glutamine side chains also help confine the nicotinamide, although we note that the conformation of Gln56 is somewhat uncertain in FbsI due to weak electron density; it is possible that this side chain samples different rotamers in the NADP+ complex. The adenosine 2'-phosphoryl of NADP+ interacts with two lysine side chains (Figure 8C). Asn264 may provide additional stabilization, although the interaction distance is long for a hydrogen bond (3.9 Å). Interestingly, Asn264 is replaced in the SsDesB and DfoA cadaverine hydroxylases by lysine, enabling them to form an additional ion pair with the adenosine 2'-phosphoryl. Finally, we note that the conserved water of the Rossmann fold⁵⁰ is present in the NADPH site of FbsI (as well as in cadaverine hydroxylase and ornithine hydroxylase). This water molecule bridges the pyrophosphate of the dinucleotide with the glycine-rich loop of the Rossmann fold (Figure 8C).

DISCUSSION

In this work, we presented the biochemical and structural characterization of the aliphatic diamine *N*-hydroxylase FbsI. The catalytic function of FbsI is essential for the biosynthesis

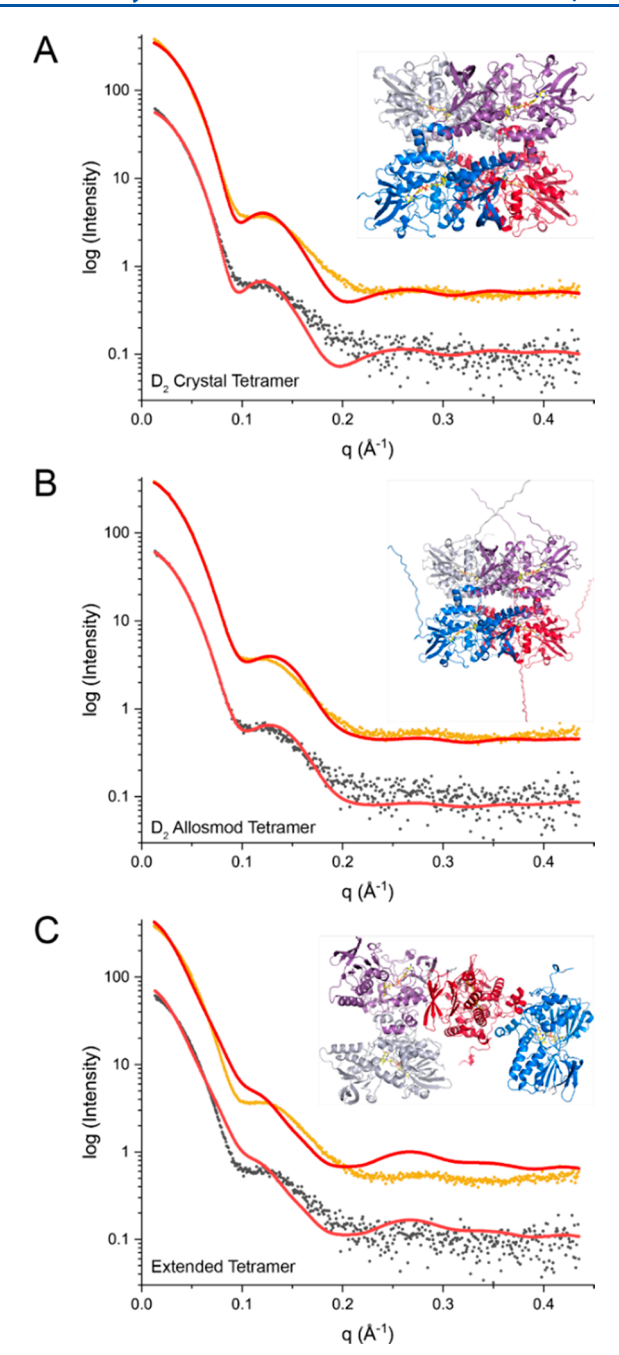


Figure 7. Comparison of the experimental SAXS curves (circles) with theoretical SAXS curves calculated from atomic models (red curves). For clarity, only the data for the lowest (1 mg/mL) and highest (9 mg/mL) protein concentrations are shown. (A) SAXS curves calculated from the crystal D_2 tetramer. (B) SAXS curves calculated from the crystal D_2 tetramer with missing residues added by AllosMod. (C) SAXS curves calculated from the extended four-body assembly present in the crystal lattice.

Table 5. Goodness-of-Fit Parameters from FoXS (χ^2) from Fitting the SAXS Data with Atomic Models

Conc. (mg/mL)	1	3	5	6	8	9
Crystal D ₂ tetramer	0.29	1.4	1.3	1.8	2.6	3.9
AllosMod D ₂ tetramer	0.090	0.32	0.33	0.57	0.84	1.1
Extended tetramer	1.8	11.2	11.6	21.0	29.3	35.0

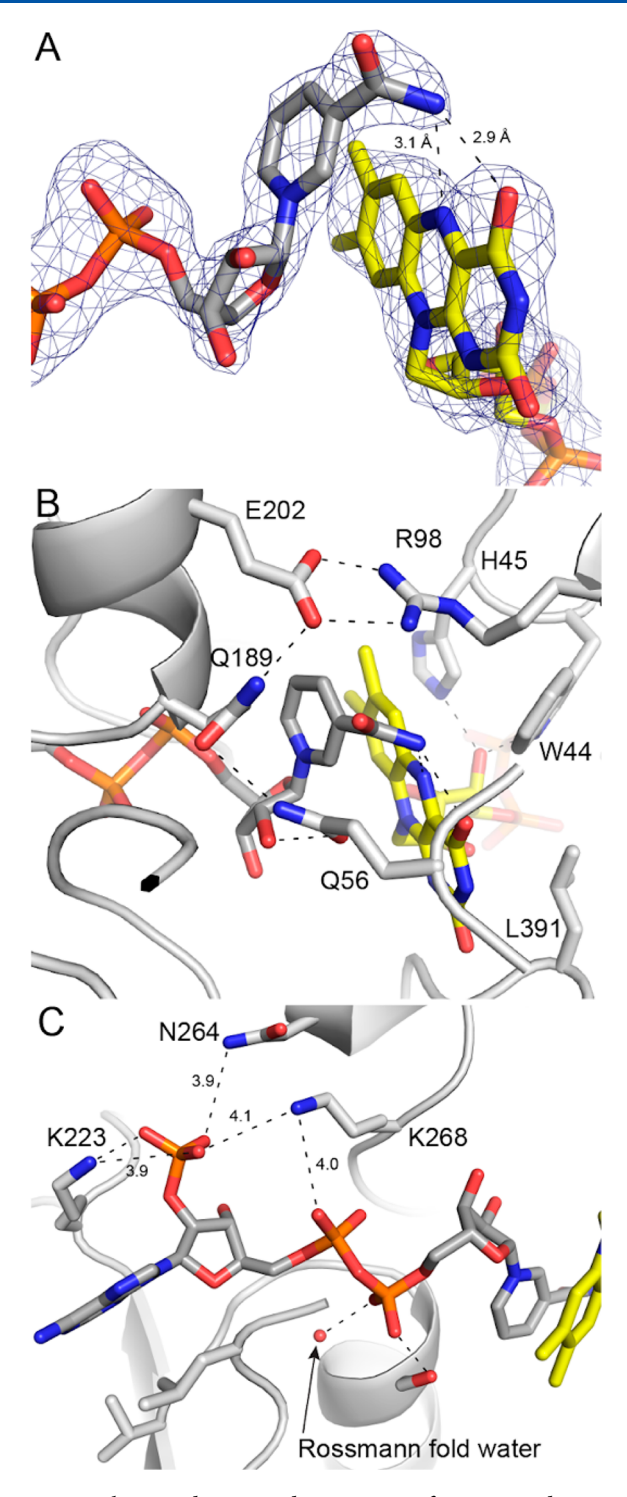


Figure 8. Electron density and interactions for FAD and NADP⁺ bound to FbsI. (A) Polder omit map for FAD (yellow) and NADP⁺ (gray) in chain D contoured at 4σ . (B) Environment around the isoalloxazine-nicotinamide interface. The dashed lines indicate interactions within a 3.2 Å cutoff. (C) Environment around the ADP part of NADP⁺. The dashed lines indicate interactions within a 3.2 Å cutoff, except where noted.

of functional fimsbactins in *A. baumannii*. The enzyme activity studies revealed that this enzyme does not use lysine or ornithine as substrates, preferring aliphatic diamines instead. Based on the catalytic efficiency values calculated with the oxygen consumption assays, putrescine is the preferred

Oxidized Flavin

Reduced Flavin

$$H_3C$$
 H_3C
 H_3

Figure 9. Proposed catalytic mechanism of FbsI. (A) The reaction starts by binding of NADPH to oxidized FbsI with relative low affinity. (B) Hydride transfer takes place, producing reduced FbsI in complex with NADP $^+$. (C) Putrescine binds and the reduced flavin reacts with molecular oxygen via an electron transfer step to "activate" the oxygen and form the C4a-hydroperoxyflavin intermediate. (D) Hydroxylation occurs, resulting in the production of N-hydroxyputrescine and a C4a-hydroxyflavin. (E) The penultimate step is flavin dehydration to reform oxidized flavin and release of hydroxylated putrescine. (F) The last step in the cycle is release of NADP $^+$. (G) If putrescine is not present in the active site or is in the incorrect orientation, then the C4a-hydroperoxyflavin intermediate will decay, releasing H_2O_2 .

substrate with a $k_{\rm cat}/K_{\rm m}$ value ~3.5-fold higher than cadaverine. Using the iodine oxidation assay that measures the amount of hydroxylated product, it was noted that the k_{cat} $K_{\rm m}$ for cadaverine decreased ~7-fold as compared to putrescine (Table 2). This decrease was mainly due to a reduction in the k_{cat} value. The difference in the k_{cat} value from the oxygen consumption assay and the iodine oxidation assay originated from uncoupling, where hydrogen peroxide is produced and no hydroxylation takes place. 51,52 This uncoupling likely takes place due to the structural similarities of cadaverine and putrescine, whereas cadaverine can fit within the active site but is likely not appropriately positioned in comparison to putrescine to the C4a of the isoalloxazine ring on the flavin, resulting in breakdown of the C4a-hydroperoxyflavin intermediate. These results are consistent with putrescine being the preferred substrate for FbsI. The $k_{\rm cat}/K_{\rm m}$ values for NADPH are ~2-fold higher than for NADH, suggesting a slight preference for NADPH. We performed product inhibition experiments with various concentrations of NADP⁺ as a function of NADPH concentrations. The doublereciprocal plot only showed changes in the slope, consistent with NADP+ binding to the same enzyme form as NADPH and being the last product to be released during catalysis.

Because FbsI is a flavin-dependent enzyme, we used stopped-flow spectrophotometry to measure the rate constant for formation and decay of the various redox intermediates in the FbsI reaction. The initial steps are the binding of NAD(P)H, reduction of the flavin, and formation of the reduced FbsI:NADP+ complex, which completes the reductive half-reaction. Flavin reduction (k_{red}) occurred in two distinct phases. The k_{red} value was approximately 8-fold higher when FbsI was reduced with NADPH vs NADH. In addition, the K_D for NADPH was 1.6-fold lower than that of NADH. These results indicate that FbsI displays a minor preference for NADPH. We also show that substrate binding has only minor effects on the rate of flavin reduction and the K_D of NADPH. The presence of two phases for flavin reduction has been previously observed in some Class B FMOs. 22,53 The fast phase, occurring within the first second, is faster than the k_{cat} measured in the steady-state kinetic assays. The slow phase,

making up approximately 25% of the amplitude change for the reduction, occurs between the first and tenth seconds of reduction. We hypothesize that this slow phase is present due to a population of FbsI that is in a different conformation partially inactive.

In the oxidative half-reaction, the reduced FbsI:NADP+ complex reacts with oxygen presumably generating a C4ahydroperoxy intermediate, which if stable, can be observed. In the absence of putrescine, an increase in absorbance at 370 nm occurred in a single phase, and this peak is characteristic of the C4a-hydroperoxy intermediate in other NMOs (Figure 4).41,54,55 This intermediate is stable and decays slowly to regenerate the oxidized flavin (monitored at 450 nm) by releasing hydrogen peroxide. When putrescine was present, formation of the C4a-hydroperoxy intermediate formation (k_{OOH}) occurred ~8-fold faster. The enhancement in the k_{OOH} value has also been observed in other NMOs. It was suggested for the related ornithine hydroxylase, SidA, that substrate binding enhances a conformational change that favors reactivity with oxygen. 56 The absorbance changes at 450 nm in the presence of putrescine occur in two phases, with the fast phase at $0.400 \pm 0.002 \text{ s}^{-1}$ and the slow phase at 0.030 ± 0.003 s^{-1} . We attribute the slow phase to a population of protein with lower activity. The fast phase is similar in value to the k_{cat} for FbsI $(0.60 \pm 0.10 \text{ s}^{-1})$. These results suggest that dehydration of the C4a-hydroxyflavin intermediate may be partially ratelimiting. Another possible explanation is that hydroxylation of putrescine, rather than flavin dehydration, could be a ratelimiting step in the oxidative half-reaction. This has been observed with some two-component flavin monooxygenase systems; however, this has not been well explored in singlecomponent FMOs. 57,58

The results from the stopped-flow kinetic analysis are consistent with FbsI belonging to the Class B NMOs, as is the crystal structure showing two Rossmann domains for binding FAD and NADPH. The catalytic cycle of this group of enzymes utilize the "bold mechanism," where flavin reduction can occur in the absence of substrate and NADP⁺ remains bound during catalysis, playing a role in the stabilization of the C4a-hydroperoxyflavin intermediate. ^{56,59} In contrast, Class A

FMOs such as *p*-hydroxybenzoate hydroxylase (PHBH) utilize the "cautious mechanism" of flavin reduction, which requires substrate binding to allow the flavin to be reduced.⁶⁰ The kinetic characterization of FbsI is consistent with the catalytic cycle shown in Figure 9.

The structure of FbsI resembles that of other members of the NMO family^{27,49,52,61,62} and provides clues about cofactor selectivity. The selectivity of FbsI for NADPH is rather small (3-fold), compared to other NMOs, which tend to show selectivity of 40-fold or higher.⁶³ For example, the SidA ornithine hydroxylase shows a 70-fold selectivity for NADPH over NADH based on the *K*_D. In both SidA and FbsI, three residues make four interactions with the 2'-phosphoryl group of NADPH; however, the strength of these interactions differs in the two enzymes (Figure S8). In SidA, the 2'-phosphoryl is stabilized by three electrostatic interactions within 3.0 Å, including a bidentate ion pair with Arg279 (Figure S8A).⁴⁹ In contrast, only one interaction is within 3.0 Å in FbsI (Figure S8B). The apparently greater stabilization of the 2'-phosphoryl in SidA may account for its greater preference for NADPH.

Attempts to obtain a structure of FbsI with putrescine were unsuccessful. Nevertheless, the structure may provide insight into substate recognition. We docked a model of putrescine into the active site of FbsI based on the structure of SidA complexed with L-ornithine (PDB ID 6X0J).64 The model predicts that Asp390 and Thr240 provide interactions that anchor the distal amino group of the substrate in the active site tunnel (Figure S9). The lack of obligate hydrogen bond donors or positively charged side chains in this region is consistent with the lack of activity with L-ornithine and L-lysine, which contain carboxylate groups. The side chains of Met230, Leu232, and Ile57 form nonpolar contacts with the aliphatic part of the substrate. The active site tunnel seems large enough to also accommodate cadaverine, which differs from putrescine by the addition of a methylene group. This is consistent with FbsI activity being observed with cadaverine.

In conclusion, we present the first kinetic and structural characterization of a flavin-dependent putrescine *N*-hydroxylase involved in siderophore biosynthesis. FbsI's high substrate selectivity for putrescine support its *in vivo* role in synthesizing fimsbactins for *A. baumannii*. Additionally, we show FbsI to belong to the Class B FMOs, based on the protein fold and the ability to reduce its flavin prosthetic group in the absence of substrate. The crystal structure further reveals similarities to other aliphatic diamine or amino-acid-catalyzing NMOs, showing conservation of this enzyme class among fungi and bacteria. SAXS and size-exclusion chromatography support crystallographic evidence that FbsI exists as a tetramer in solution at concentrations of 1 mg/mL or higher. Future studies probing substrate selectivity will further elucidate the mechanism of FbsI and facilitate inhibitor discovery.

ASSOCIATED CONTENT

Data Availability Statement

All processed data are included in this manuscript. Requests for raw data, further information, or reagents contained within the manuscript are available upon request from the corresponding authors.

Supporting Information

The Supporting Information is available free of charge at https://pubs.acs.org/doi/10.1021/acs.biochem.2c00493.

Comparison of sequence identity of similar NMOs to FbsI. Overview of protein purification and size-exclusion chromatography. Results of NADP⁺ inhibition study. LC-MS chromatograms for Fmoc-Cl derivatization. Comparison of structural alignments of solved crystal structures to FbsI along with electron density maps for FAD and NADP⁺. SAXS curves for varying FbsI concentrations. Active site architectures identifying residues potentially involved in cofactor and putrescine binding (PDF)

Accession Codes

FbsI WP_001088061.1 (NCBI), SsDesB C9Z469 (NCBI), DfoA CBA23306 (NCBI), SidA AAT84594 (NCBI). All PDB and SASBDB accession codes are provided in the main text.

AUTHOR INFORMATION

Corresponding Authors

Pablo Sobrado — Department of Biochemistry and Center for Drug Discovery, Virginia Tech, Blacksburg, Virginia 24061, United States; orcid.org/0000-0003-1494-5382; Email: psobrado@vt.edu

John J. Tanner — Department of Biochemistry, University of Missouri, Columbia, Missouri 65211, United States; Department of Chemistry, University of Missouri, Columbia, Missouri 65211, United States; ◎ orcid.org/0000-0001-8314-113X; Email: tannerjj@missouri.edu

Authors

Noah S. Lyons – Department of Biochemistry and Center for Drug Discovery, Virginia Tech, Blacksburg, Virginia 24061, United States; orcid.org/0000-0003-2566-5087

Alexandra N. Bogner — Department of Biochemistry, University of Missouri, Columbia, Missouri 65211, United States; Occid.org/0000-0002-0358-422X

Complete contact information is available at: https://pubs.acs.org/10.1021/acs.biochem.2c00493

Author Contributions

A.N.B. and N.S.L.: Methodology, Investigation, Writing-Original Draft, Writing-Review & Editing, Visualization. P.S. and J.J.T.: Conceptualization, Formal analysis, Writing-Original Draft, Writing-Review & Editing, Visualization, Validation, Supervision, Project administration, Funding acquisition.

Funding

This research was supported by National Science Foundation grants CHE-2003658 (to P.S.) and CHE-2003986 (to J.J.T.).

Notes

The authors declare no competing financial interest.

ACKNOWLEDGMENTS

We would like to thank Dr. Timothy Wencewicz and Jinping Yang from Washington University, St. Louis, MO for providing the plasmid for expression of FbsI and for helpful discussion. We also thank Drs. Rich Helm and Sherry Hildreth at the Virginia Tech Mass Spectrometry Incubator (MSI) for their assistance in performing and analyzing the LC-MS product detection experiments. N.S.L. was supported, in part, by the Cunningham Doctoral Fellowship from Graduate School at Virginia Tech. We thank Jonathan Schuermann for assistance with X-ray diffraction data collection and processing. We thank Greg Hura and Kathryn Burnett for assistance with SAXS data

collection and processing. X-ray diffraction data collection and processing were conducted at the Northeastern Collaborative Access Team beamlines, which are funded by the National Institute of General Medical Sciences from the National Institutes of Health (P30 GM124165). The Eiger 16M detector on 24-ID-E is funded by a NIH-ORIP HEI grant (S10OD021527). This research used resources of the Advanced Photon Source, a U.S. Department of Energy (DOE) Office of Science User Facility operated for the DOE Office of Science by Argonne National Laboratory under Contract No. DE-AC02-06CH11357. SAXS experiments were conducted at the Advanced Light Source (ALS), a national user facility operated by Lawrence Berkeley National Laboratory on behalf of the Department of Energy, Office of Basic Energy Sciences, through the Integrated Diffraction Analysis Technologies (IDAT) program, supported by DOE Office of Biological and Environmental Research. Additional support comes from the National Institute of Health project ALS-ENABLE (P30 GM124169) and a High-End Instrumentation Grant S10OD018483.

ABBREVIATIONS

FMO, flavin-dependent monooxygenase; NHP, N-hydroxyputrescine; NMO, N-hydroxylating monooxygenase; NRPS, nonribosomal peptide synthase; FMOs, flavin monooxygenases; SAXS, small-angle X-ray scattering

REFERENCES

- (1) Lee, C. R.; Lee, J. H.; Park, M.; Park, K. S.; Bae, I. K.; Kim, Y. B.; Cha, C. J.; Jeong, B. C.; Lee, S. H. Biology of Acinetobacter baumannii: Pathogenesis, Antibiotic Resistance Mechanisms, and Prospective Treatment Options. *Front. Cell. Infect. Microbiol.* **2017**, *7*, 55.
- (2) Vincent, J. L.; Rello, J.; Marshall, J.; Silva, E.; Anzueto, A.; Martin, C. D.; Moreno, R.; Lipman, J.; Gomersall, C.; Sakr, Y.; Reinhart, K.; Investigators, E. I. G. o. International study of the prevalence and outcomes of infection in intensive care units. *JAMA* **2009**, 302 (21), 2323–9.
- (3) Peleg, A. Y.; Seifert, H.; Paterson, D. L. Acinetobacter baumannii: emergence of a successful pathogen. *Clin Microbiol Rev.* **2008**, 21 (3), 538–82.
- (4) Vrancianu, C. O.; Gheorghe, I.; Czobor, I. B.; Chifiriuc, M. C. Antibiotic Resistance Profiles, Molecular Mechanisms and Innovative Treatment Strategies of Acinetobacter baumannii. *Microorganisms* **2020**, *8* (6), 935.
- (5) Dijkshoorn, L.; Nemec, A.; Seifert, H. An increasing threat in hospitals: multidrug-resistant Acinetobacter baumannii. *Nat. Rev. Microbiol.* **2007**, *5* (12), 939–51.
- (6) Fischbach, M. A.; Lin, H.; Liu, D. R.; Walsh, C. T. How pathogenic bacteria evade mammalian sabotage in the battle for iron. *Nat. Chem. Biol.* **2006**, 2 (3), 132–8.
- (7) Yamamoto, S.; Okujo, N.; Sakakibara, Y. Isolation and structure elucidation of acinetobactin, a novel siderophore from Acinetobacter baumannii. *Arch. Microbiol.* **1994**, *162* (4), 249–54.
- (8) Penwell, W. F.; DeGrace, N.; Tentarelli, S.; Gauthier, L.; Gilbert, C. M.; Arivett, B. A.; Miller, A. A.; Durand-Reville, T. F.; Joubran, C.; Actis, L. A. Discovery and Characterization of New Hydroxamate Siderophores, Baumannoferrin A and B, produced by Acinetobacter baumannii. *Chembiochem* **2015**, *16* (13), 1896–1904.
- (9) Proschak, A.; Lubuta, P.; Grun, P.; Lohr, F.; Wilharm, G.; De Berardinis, V.; Bode, H. B. Structure and biosynthesis of fimsbactins A-F, siderophores from Acinetobacter baumannii and Acinetobacter baylyi. *Chembiochem* **2013**, *14* (5), *633*–8.
- (10) Brender, J. R.; Dertouzos, J.; Ballou, D. P.; Massey, V.; Palfey, B. A.; Entsch, B.; Steel, D. G.; Gafni, A. Conformational dynamics of

- the isoalloxazine in substrate-free p-hydroxybenzoate hydroxylase: single-molecule studies. J. Am. Chem. Soc. 2005, 127 (51), 18171–8.
- (11) Eijkelkamp, B. A.; Hassan, K. A.; Paulsen, I. T.; Brown, M. H. Investigation of the human pathogen Acinetobacter baumannii under iron limiting conditions. *BMC Genomics* **2011**, *12*, 126.
- (12) D'Onofrio, A.; Crawford, J. M.; Stewart, E. J.; Witt, K.; Gavrish, E.; Epstein, S.; Clardy, J.; Lewis, K. Siderophores from neighboring organisms promote the growth of uncultured bacteria. *Chem. Biol.* **2010**, *17* (3), 254–64.
- (13) McRose, D. L.; Seyedsayamdost, M. R.; Morel, F. M. M. Multiple siderophores: bug or feature? *J. Biol. Inorg. Chem.* **2018**, 23 (7), 983–993.
- (14) Bohac, T. J.; Fang, L.; Giblin, D. E.; Wencewicz, T. A. Fimsbactin and Acinetobactin Compete for the Periplasmic Siderophore Binding Protein BauB in Pathogenic Acinetobacter baumannii. ACS Chem. Biol. 2019, 14 (4), 674–687.
- (15) Sheldon, J. R.; Skaar, E. P. Acinetobacter baumannii can use multiple siderophores for iron acquisition, but only acinetobactin is required for virulence. *PLoS Pathog.* **2020**, *16* (10), No. e1008995.
- (16) Mugge, C.; Heine, T.; Baraibar, A. G.; van Berkel, W. J. H.; Paul, C. E.; Tischler, D. Flavin-dependent N-hydroxylating enzymes: distribution and application. *Appl. Microbiol. Biotechnol.* **2020**, *104* (15), 6481–6499.
- (17) Huijbers, M. M.; Montersino, S.; Westphal, A. H.; Tischler, D.; van Berkel, W. J. Flavin dependent monooxygenases. *Arch. Biochem. Biophys.* **2014**, *544*, 2–17.
- (18) Chapman, S. K.; Reid, G. A. Flavoprotein Protocols; Humana Press, 1999; Vol. 131, pp 5-7.
- (19) Oppenheimer, M.; Poulin, M. B.; Lowary, T. L.; Helm, R. F.; Sobrado, P. Characterization of recombinant UDP-galactopyranose mutase from Aspergillus fumigatus. *Arch. Biochem. Biophys.* **2010**, *502* (1), 31–8.
- (20) Chocklett, S. W.; Sobrado, P. Aspergillus fumigatus SidA is a highly specific ornithine hydroxylase with bound flavin cofactor. *Biochemistry* **2010**, 49 (31), 6777–83.
- (21) Csáky, T. Z.; Hassel, O.; Rosenberg, T.; Lång, S.; Turunen, E.; Tuhkanen, A. On the Estimation of Bound Hydroxylamine in Biological Materials. *Acta Chem. Scand.* **1948**, 2 (2), 450–454.
- (22) Robinson, R. M.; Rodriguez, P. J.; Sobrado, P. Mechanistic studies on the flavin-dependent N(6)-lysine monooxygenase MbsG reveal an unusual control for catalysis. *Arch. Biochem. Biophys.* **2014**, 550–551, 58–66.
- (23) Valentino, H.; Sobrado, P. Performing anaerobic stopped-flow spectrophotometry inside of an anaerobic chamber. *Methods Enzymol* **2019**, *620*, 51–88.
- (24) Kabsch, W. XDS. Acta Crystallogr. D Biol. Crystallogr. 2010, 66 (2), 125–132.
- (25) Evans, P. R.; Murshudov, G. N. How good are my data and what is the resolution? *Acta Crystallogr. D Biol. Crystallogr.* **2013**, 69 (7), 1204–1214.
- (26) Matthews, B. W. Solvent content of protein crystals. *J. Mol. Biol.* **1968**, 33 (2), 491–7.
- (27) Giddings, L. A.; Lountos, G. T.; Kim, K. W.; Brockley, M.; Needle, D.; Cherry, S.; Tropea, J. E.; Waugh, D. S. Characterization of a broadly specific cadaverine N-hydroxylase involved in desferrioxamine B biosynthesis in Streptomyces sviceus. *PLoS One* **2021**, *16* (3), No. e0248385.
- (28) Leferink, N. G.; Heuts, D. P.; Fraaije, M. W.; van Berkel, W. J. The growing VAO flavoprotein family. *Archives of biochemistry and biophysics* **2008**, 474 (2), 292–301.
- (29) Adams, P. D.; Afonine, P. V.; Bunkoczi, G.; Chen, V. B.; Echols, N.; Headd, J. J.; Hung, L. W.; Jain, S.; Kapral, G. J.; Grosse Kunstleve, R. W.; McCoy, A. J.; Moriarty, N. W.; Oeffner, R. D.; Read, R. J.; Richardson, D. C.; Richardson, J. S.; Terwilliger, T. C.; Zwart, P. H. The Phenix software for automated determination of macromolecular structures. *Methods* **2011**, *55* (1), 94–106.
- (30) McCoy, A. J. Solving structures of protein complexes by molecular replacement with Phaser. *Acta Crystallogr. D Biol. Crystallogr.* **2007**, 63 (1), 32–41.

- (31) Emsley, P.; Cowtan, K. Coot: model-building tools for molecular graphics. *Acta Crystallogr. D Biol. Crystallogr.* **2004**, *60* (12), 2126–2132.
- (32) Liebschner, D.; Afonine, P. V.; Moriarty, N. W.; Poon, B. K.; Sobolev, O. V.; Terwilliger, T. C.; Adams, P. D. Polder maps: improving OMIT maps by excluding bulk solvent. *Acta Crystallogr. D Struct. Biol.* **2017**, *73* (2), 148–157.
- (33) Adams, P. D.; Afonine, P. V.; Bunkoczi, G.; Chen, V. B.; Davis, I. W.; Echols, N.; Headd, J. J.; Hung, L. W.; Kapral, G. J.; Grosse-Kunstleve, R. W.; McCoy, A. J.; Moriarty, N. W.; Oeffner, R.; Read, R. J.; Richardson, D. C.; Richardson, J. S.; Terwilliger, T. C.; Zwart, P. H. PHENIX: a comprehensive Python-based system for macromolecular structure solution. *Acta Crystallogr. D Biol. Crystallogr.* 2010, 66 (2), 213–221.
- (34) Gore, S.; Sanz Garcia, E.; Hendrickx, P. M. S.; Gutmanas, A.; Westbrook, J. D.; Yang, H.; Feng, Z.; Baskaran, K.; Berrisford, J. M.; Hudson, B. P.; Ikegawa, Y.; Kobayashi, N.; Lawson, C. L.; Mading, S.; Mak, L.; Mukhopadhyay, A.; Oldfield, T. J.; Patwardhan, A.; Peisach, E.; Sahni, G.; Sekharan, M. R.; Sen, S.; Shao, C.; Smart, O. S.; Ulrich, E. L.; Yamashita, R.; Quesada, M.; Young, J. Y.; Nakamura, H.; Markley, J. L.; Berman, H. M.; Burley, S. K.; Velankar, S.; Kleywegt, G. J. Validation of Structures in the Protein Data Bank. *Structure* 2017, 25 (12), 1916–1927.
- (35) Dyer, K. N.; Hammel, M.; Rambo, R. P.; Tsutakawa, S. E.; Rodic, I.; Classen, S.; Tainer, J. A.; Hura, G. L. High-throughput SAXS for the characterization of biomolecules in solution: a practical approach. *Methods Mol. Biol., Clifton, N.I.* 2014, 1091, 245–58.
- (36) Konarev, P. V.; Volkov, V. V.; Sokolova, A. V.; Koch, M. H. J.; Svergun, D. I. PRIMUS: a Windows PC-based system for small-angle scattering data analysis. *J. Appl. Crystallogr.* **2003**, 36 (5), 1277–1282.
- (37) Piiadov, V.; Ares de Araujo, E.; Oliveira Neto, M.; Craievich, A. F.; Polikarpov, I. SAXSMoW 2.0: Online calculator of the molecular weight of proteins in dilute solution from experimental SAXS data measured on a relative scale. *Protein Sci.* 2019, 28 (2), 454–463.
- (38) Schneidman-Duhovny, D.; Hammel, M.; Sali, A. FoXS: a web server for rapid computation and fitting of SAXS profiles. *Nucleic Acids Res.* **2010**, 38, W540–W544.
- (39) Kikhney, A. G.; Borges, C. R.; Molodenskiy, D. S.; Jeffries, C. M.; Svergun, D. I. SASBDB: Towards an automatically curated and validated repository for biological scattering data. *Protein Sci.* **2020**, 29 (1), 66–75.
- (40) Chaiyen, P.; Fraaije, M. W.; Mattevi, A. The enigmatic reaction of flavins with oxygen. *Trends in biochemical sciences* **2012**, 37 (9), 373–80.
- (41) Han, A.; Robinson, R. M.; Badieyan, S.; Ellerbrock, J.; Sobrado, P. Tryptophan-47 in the active site of Methylophaga sp. strain SK1 flavin-monooxygenase is important for hydride transfer. *Arch. Biochem. Biophys.* **2013**, 532 (1), 46–53.
- (42) van Berkel, W. J.; Kamerbeek, N. M.; Fraaije, M. W. Flavoprotein monooxygenases, a diverse class of oxidative biocatalysts. *Journal of biotechnology* **2006**, *124* (4), 670–89.
- (43) Krissinel, E.; Henrick, K. Secondary-structure matching (SSM), a new tool for fast protein structure alignment in three dimensions. *Acta Crystallogr. D Biol. Crystallogr.* **2004**, *60* (12), 2256–68.
- (44) Krissinel, E.; Henrick, K. Inference of macromolecular assemblies from crystalline state. *J. Mol. Biol.* **2007**, 372 (3), 774–97.
- (45) Meneely, K. M.; Lamb, A. L. Biochemical characterization of a flavin adenine dinucleotide-dependent monooxygenase, ornithine hydroxylase from Pseudomonas aeruginosa, suggests a novel reaction mechanism. *Biochemistry* **2007**, *46* (42), 11930–7.
- (46) Hajizadeh, N. R.; Franke, D.; Jeffries, C. M.; Svergun, D. I. Consensus Bayesian assessment of protein molecular mass from solution X-ray scattering data. *Sci. Rep.* **2018**, 8 (1), 7204.
- (47) Schneidman-Duhovny, D.; Kim, S. J.; Sali, A. Integrative structural modeling with small angle X-ray scattering profiles. *BMC Struc. Biol.* **2012**, *12*, 17.
- (48) Guttman, M.; Weinkam, P.; Sali, A.; Lee, K. K. All-atom ensemble modeling to analyze small-angle x-ray scattering of glycosylated proteins. *Structure* **2013**, 21 (3), 321–31.

- (49) Campbell, A. C.; Robinson, R.; Mena-Aguilar, D.; Sobrado, P.; Tanner, J. J. Structural Determinants of Flavin Dynamics in a Class B Monooxygenase. *Biochemistry* **2020**, *59* (48), 4609–4616.
- (50) Bottoms, C. A.; Smith, P. E.; Tanner, J. J. A structurally conserved water molecule in Rossmann dinucleotide-binding domains. *Protein Soc.* **2002**, *11* (9), 2125–37.
- (51) Abdelwahab, H.; Robinson, R.; Rodriguez, P.; Adly, C.; El-Sohaimy, S.; Sobrado, P. Identification of structural determinants of NAD(P)H selectivity and lysine binding in lysine N(6)-monooxygenase. *Arch. Biochem. Biophys.* **2016**, *606*, 180–8.
- (52) Binda, C.; Robinson, R. M.; Martin Del Campo, J. S.; Keul, N. D.; Rodriguez, P. J.; Robinson, H. H.; Mattevi, A.; Sobrado, P. An Unprecedented NADPH Domain Conformation in Lysine Monooxygenase NbtG Provides Insights into Uncoupling of Oxygen Consumption from Substrate Hydroxylation. *J. Biol. Chem.* **2015**, 290 (20), 12676–88.
- (53) Valentino, H.; Campbell, A. C.; Schuermann, J. P.; Sultana, N.; Nam, H. G.; LeBlanc, S.; Tanner, J. J.; Sobrado, P. Structure and function of a flavin-dependent S-monooxygenase from garlic (*Allium satvium*). *J. Biol. Chem.* **2020**, 295 (32), 11042–11055.
- (54) Shirey, C.; Badieyan, S.; Sobrado, P. Role of Ser-257 in the sliding mechanism of NADP(H) in the reaction catalyzed by the Aspergillus fumigatus flavin-dependent ornithine N5-monooxygenase SidA. J. Biol. Chem. 2013, 288 (45), 32440–8.
- (55) Sobrado, P. Flavin-Dependent N-Hydroxylating monooxygenases in Bacterial and Fungi Siderophore Biosynthesis. In *Flavins and Flavoproteins 2011*; Miller, S., Hille, R., Palfey, B., Eds.; Lulu.com, 2013; pp 265–276.
- (56) Robinson, R.; Badieyan, S.; Sobrado, P. C4a-hydroperoxyflavin formation in N-hydroxylating flavin monooxygenases is mediated by the 2'-OH of the nicotinamide ribose of NADP(+). *Biochemistry* **2013**, 52 (51), 9089–91.
- (57) Ruangchan, N.; Tongsook, C.; Sucharitakul, J.; Chaiyen, P. pH-dependent Studies Reveal an Efficient Hydroxylation Mechanism of the Oxygenase Component of p-Hydroxyphenylacetate 3-Hydroxylase. *J. Biol. Chem.* **2011**, 286 (1), 223–233.
- (58) Pimviriyakul, P.; Thotsaporn, K.; Sucharitakul, J.; Chaiyen, P. Kinetic Mechanism of the Dechlorinating Flavin-Dependent Monooxygenase HadA. *J. Biol. Chem.* **2017**, 292 (12), 4818–4832.
- (59) Alfieri, A.; Malito, E.; Orru, R.; Fraaije, M. W.; Mattevi, A. Revealing the moonlighting role of NADP in the structure of a flavin-containing monooxygenase. *Proc. Natl. Acad. Sci. U.S.A.* **2008**, *105* (18), 6572–7.
- (60) Entsch, B.; van Berkel, W. J. Structure and mechanism of parahydroxybenzoate hydroxylase. FASEB J. 1995, 9 (7), 476–83.
- (61) Olucha, J.; Lamb, A. L. Mechanistic and structural studies of the N-hydroxylating flavoprotein monooxygenases. *Bioorganic chemistry* **2011**, 39 (5–6), 171–7.
- (62) Franceschini, S.; Fedkenheuer, M.; Vogelaar, N. J.; Robinson, H. H.; Sobrado, P.; Mattevi, A. Structural insight into the mechanism of oxygen activation and substrate selectivity of flavin-dependent N-hydroxylating monooxygenases. *Biochemistry* **2012**, *51* (36), 7043–5.
- (63) Romero, E.; Fedkenheuer, M.; Chocklett, S. W.; Qi, J.; Oppenheimer, M.; Sobrado, P. Dual role of NADP(H) in the reaction of a flavin dependent N-hydroxylating monooxygenase. *Biochim. Biophys. Acta* **2012**, 1824 (6), 850–7.
- (64) Campbell, A. C.; Stiers, K. M.; Martin del Campo, J. S.; Mehra-Chaudhary, R.; Sobrado, P.; Tanner, J. J. Trapping conformational states of a flavin-dependent N-moonoxygenase in crystallo reveals protein and flavin dynamics. *J. Biol. Chem.* **2020**, 295 (38), 13239–49.